

---

# A MULTI-PHYSICS SIMULATION FRAMEWORK FOR HIGH-POWER MICROWAVE COUNTER-UNMANNED AERIAL SYSTEM DESIGN AND PERFORMANCE EVALUATION \*

---

A. A. Jafari  
 University of Tartu  
 Tartu, Estonia  
 akbar.anbar.jafari@ut.ee

G. Anbarjafari  
 3S Holding OÜ  
 Tartu, Estonia  
 shb@3sholding.com

## ABSTRACT

The proliferation of small unmanned aerial systems (sUAS) operating under autonomous guidance has created an urgent need for non-kinetic neutralization methods that are immune to conventional radio-frequency jamming. This paper presents a comprehensive multi-physics simulation framework for the design and performance evaluation of a high-power microwave (HPM) counter-UAS system operating at 2.45 GHz. The framework integrates electromagnetic propagation modelling, antenna pattern analysis, electromagnetic coupling to unshielded drone wiring harnesses, and a sigmoid-based semiconductor damage probability model calibrated to published CMOS latchup thresholds. A 10,000-trial Monte Carlo analysis incorporating stochastic variations in transmitter power, antenna pointing error, target wire orientation, polarization mismatch, and component damage thresholds yields system-level kill probabilities with 95% confidence intervals. For a baseline configuration of 25 kW continuous-wave power and a 60 cm parabolic reflector (21.2 dBi gain), the Monte Carlo simulation predicts a kill probability of  $51.4 \pm 1.0\%$  at 20 m, decreasing to  $13.1 \pm 0.7\%$  at 40 m. Pulsed operation at 500 kW peak power (1% duty cycle) extends the 90% kill range from approximately 18 m to 88 m. The framework further provides parametric design maps, safety exclusion zone calculations compliant with ICNIRP 2020 guidelines, thermal management requirements, and waveguide mode analysis. All simulation codes and results are provided for full reproducibility.

**Keywords** high-power microwave · counter-UAS · directed energy weapon · CMOS latchup · Monte Carlo simulation · electromagnetic coupling · drone neutralization

## 1 Introduction

The rapid proliferation of small unmanned aerial systems (sUAS) in both commercial and military domains has created asymmetric threats that challenge conventional air defence architectures [1–4]. Modern consumer drones in the 250 g to 25 kg class are inexpensive, widely available, and increasingly capable of autonomous operation using pre-programmed GPS/INS waypoints or visual navigation [5–7]. In conflict zones such as Ukraine, swarms of low-cost drones have demonstrated their ability to overwhelm conventional defences, with fiber-optic guided variants rendering traditional RF jamming entirely ineffective [8, 9].

Counter-UAS (C-UAS) technologies broadly fall into kinetic (missiles, projectiles, nets) and non-kinetic (jamming, spoofing, directed energy) categories [10–12]. Kinetic solutions suffer from finite magazine depth, high cost-per-engagement, and collateral damage risk. RF jamming, while cost-effective, is fundamentally limited against autonomous drones that do not rely on a communication link [8]. High-energy laser (HEL) systems offer precision engagement but require sustained dwell time, clear atmospheric conditions, and can only engage one target at a time [13, 14].

---

\*This work is submitted for review to *Journal of Defence Technology*.

High-power microwave (HPM) directed energy weapons offer a compelling alternative by delivering electromagnetic energy that couples directly into onboard electronic circuits, inducing semiconductor failure independent of the drone's software architecture or communication protocol [15, 16]. Unlike jamming, HPM causes a *physics-layer kill*: the irreversible destruction of MOSFET gate oxides, triggering of CMOS parasitic thyristor latchup, and thermal burnout of integrated circuit junctions [17–20]. Recent operational deployments of HPM C-UAS systems—notably the Epirus Leonidas, which achieved a 100% success rate against a 49-drone swarm in 2024 field testing, and the Raytheon Phaser—have validated the technology at system level [12].

Despite these advances, the open literature lacks a comprehensive, reproducible simulation framework that integrates all relevant physics—from RF source characteristics through electromagnetic propagation, coupling to target wiring, and probabilistic semiconductor damage—into a unified design tool. Prior work has addressed individual aspects: Bäckström and Lovstrand [16] compiled measured susceptibility thresholds; Nitsch et al. [21] characterized equipment-level responses; Wang et al. [22] provided SPICE-level CMOS latchup analysis; and Yu et al. [23] modelled frequency-dependent upset susceptibility. Recent studies have extended damage characterization to GaN HEMTs [24–28] and ESC-specific failure modes [29]. However, no prior work has synthesized these elements into a parametric design framework specifically targeting the counter-UAS application with stochastic uncertainty quantification.

This paper addresses this gap by developing a multi-physics simulation framework for HPM C-UAS system design and performance evaluation. The principal contributions are as follows:

1. A unified analytical model linking RF source parameters, antenna design, free-space propagation, and electromagnetic coupling to unshielded drone wiring to predict the induced electric field and voltage at target electronic subsystems.
2. A subsystem-resolved sigmoid damage probability model for five drone electronic subsystems (ESC, flight controller, GPS/GNSS, camera, BMS), parameterised from published experimental data.
3. A 10,000-trial Monte Carlo analysis that propagates uncertainties in transmitter power, antenna pointing, target orientation, wire geometry, and component vulnerability to produce system-level kill probabilities with confidence intervals.
4. Parametric design maps (power–aperture trade space) and safety compliance analysis against ICNIRP 2020 guidelines [30, 31].
5. Full release of all simulation source code for reproducibility.

The remainder of this paper is organized as follows. Section 2 presents the system architecture and mathematical models. Section 3 describes the simulation framework and its implementation. Section 4 presents the simulation results, including parametric analyses, Monte Carlo uncertainty quantification, and safety zone calculations. Section 5 discusses the implications, limitations, and comparison with fielded systems. Section 6 concludes the paper.

## 2 System Model

### 2.1 System architecture

The proposed HPM C-UAS system comprises six principal subsystems: (i) an AC/DC power supply unit (PSU), (ii) a high-voltage (HV) modulator providing both continuous-wave (CW) and pulsed operating modes, (iii) a cavity magnetron RF source at 2.45 GHz, (iv) a WR-340 waveguide transmission line with a ferrite circulator for source protection, (v) a parabolic reflector antenna, and (vi) a tracking subsystem incorporating an FMCW radar and an EO/IR camera on a motorized gimbal. The system-level block diagram is presented in Fig. 1.

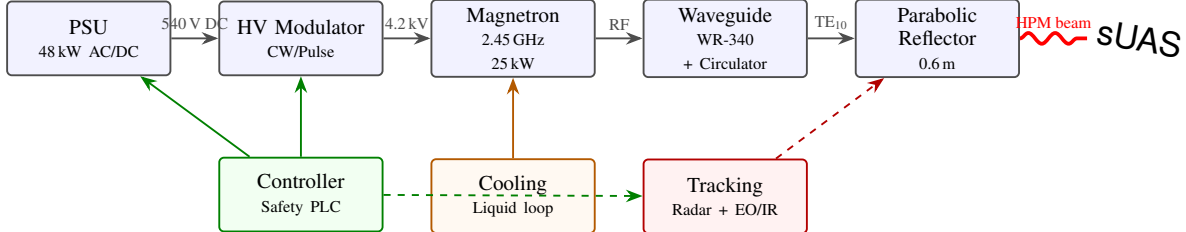


Figure 1: Top-level block diagram of the HPM counter-UAS system architecture showing the RF power chain (top), control and support subsystems (bottom), and the directed HPM beam toward the target sUAS.

The operating frequency of 2.45 GHz is selected for several reasons: it lies within the Industrial, Scientific and Medical (ISM) band, minimizing regulatory complexity; commodity cavity magnetrons at this frequency achieve 65–75% DC-to-RF conversion efficiency [32–35]; and the corresponding wavelength  $\lambda_0 = c/f_0 = 12.24$  cm ensures that typical drone wiring harnesses (5–30 cm) represent a significant fraction of  $\lambda/2$ , maximizing electromagnetic coupling [36].

## 2.2 RF propagation model

The power density  $S$  at range  $R$  from a directive antenna with gain  $G_{\text{tx}}$  is given by the Friis transmission relation:

$$S(R) = \frac{P_{\text{tx}} \cdot \eta_{\text{line}} \cdot G_{\text{tx}}}{4\pi R^2} \quad [\text{W/m}^2] \quad (1)$$

where  $P_{\text{tx}}$  is the transmitter output power and  $\eta_{\text{line}} = \eta_{\text{wg}} \cdot \eta_{\text{feed}} \cdot \eta_{\text{radome}}$  is the aggregate transmission line efficiency. The corresponding free-space electric field magnitude is:

$$|\mathbf{E}(R)| = \sqrt{S(R) \cdot \eta_0} = \sqrt{\frac{P_{\text{tx}} \cdot \eta_{\text{line}} \cdot G_{\text{tx}} \cdot \eta_0}{4\pi R^2}} \quad [\text{V/m}] \quad (2)$$

where  $\eta_0 = \sqrt{\mu_0/\epsilon_0} \approx 377 \Omega$  is the impedance of free space. The parabolic reflector gain is:

$$G_{\text{tx}} = \eta_{\text{ap}} \left( \frac{\pi D}{\lambda_0} \right)^2 \quad (3)$$

where  $D$  is the dish diameter and  $\eta_{\text{ap}}$  is the aperture efficiency (taken as 0.55 for a front-fed paraboloid with standard illumination taper). The half-power ( $-3$  dB) beamwidth is approximated as  $\theta_{3\text{dB}} \approx 70\lambda_0/D$ . For the baseline configuration ( $D = 0.60$  m), this yields  $G_{\text{tx}} = 21.2$  dBi and  $\theta_{3\text{dB}} = 14.3^\circ$ .

## 2.3 Electromagnetic coupling to target electronics

Consumer sUAS platforms are electromagnetically unshielded: flight controller PCBs, electronic speed controllers (ESCs), GPS receivers, and cameras are mounted in plastic airframes with wire harnesses acting as unintentional receiving antennas [16, 37]. The induced open-circuit voltage on a wire of physical length  $L$  illuminated by an incident electric field  $E_{\text{inc}}$  can be modelled as a short dipole when  $L < \lambda/2$ :

$$V_{\text{ind}} = E_{\text{inc}} \cdot L_{\text{eff}} \cdot F(\theta_{\text{wire}}) \cdot \sqrt{\eta_{\text{pol}}} \quad (4)$$

where  $L_{\text{eff}} = L/2$  is the effective length of a short dipole,  $F(\theta_{\text{wire}})$  accounts for the wire orientation relative to the incident polarisation, and  $\eta_{\text{pol}}$  represents the polarisation mismatch efficiency. Near the half-wave resonance ( $L \approx \lambda_0/2 = 6.12$  cm), the coupling is enhanced by the antenna quality factor  $Q$ , modelled as a Gaussian resonance peak [36]:

$$V_{\text{res}} = V_{\text{ind}} \cdot \left[ 1 + (Q - 1) \exp \left( -\frac{(L - \lambda_0/2)^2}{2\sigma_L^2} \right) \right] \quad (5)$$

with  $Q \approx 10$  and  $\sigma_L = 0.02$  m for typical unshielded harnesses. This resonance-enhanced coupling model predicts that wires in the 5–8 cm range (common for ESC signal harnesses) experience 5–10 $\times$  greater induced voltage than wires of other lengths at 2.45 GHz.

## 2.4 Semiconductor damage probability model

The probability of damage to a semiconductor subsystem exposed to an electric field of magnitude  $|E|$  is modelled by a sigmoid (logistic) function [16, 17]:

$$P_{\text{kill}}(|E|) = \frac{1}{1 + \exp \left( -\frac{|E| - E_{50}}{\sigma_E} \right)} \quad (6)$$

where  $E_{50}$  is the electric field intensity at which the damage probability equals 50%, and  $\sigma_E$  controls the steepness of the transition. This functional form is well-established in electromagnetic susceptibility analysis and captures the stochastic variability in device manufacturing, operating state, and coupling efficiency [16, 21].

Table 1 summarises the damage model parameters for the five principal drone electronic subsystems, derived from published experimental and simulation studies.

Table 1: Semiconductor damage model parameters for sUAS electronic subsystems. The parameter  $E_{50}$  represents the 50% damage threshold and  $\sigma_E$  the transition width.

Subsystem	Failure mode	$E_{50}$ [V/m]	$\sigma_E$ [V/m]	Source
GPS/GNSS LNA	Front-end burnout	150	30	[16, 21]
Flight controller	CMOS latchup	250	50	[18, 19, 38]
ESC (gate oxide)	MOSFET $V_{bd}$	300	60	[20, 29]
Camera (CMOS)	Pixel array damage	200	40	[16]
BMS MOSFET	Gate oxide failure	350	70	[17, 22]

A drone is considered neutralised if *any one* of its critical subsystems is damaged, since the loss of either motor control (ESC failure), flight stabilisation (flight controller failure), or navigation (GPS failure) results in an uncontrolled descent. The system-level kill probability is therefore:

$$P_{\text{system}}(|E|) = 1 - \prod_{i=1}^N [1 - P_{\text{kill},i}(|E|)] \quad (7)$$

where the product extends over all  $N$  vulnerable subsystems.

## 2.5 Waveguide transmission analysis

The RF power is transported from the magnetron to the feed horn through a WR-340 rectangular waveguide ( $a = 86.36$  mm,  $b = 43.18$  mm). The cutoff frequency of the dominant  $\text{TE}_{10}$  mode is:

$$f_{c,10} = \frac{c}{2a} = \frac{2.998 \times 10^8}{2 \times 0.08636} = 1.736 \text{ GHz} \quad (8)$$

At the operating frequency of 2.45 GHz, only the  $\text{TE}_{10}$  mode propagates, since the next mode ( $\text{TE}_{20}$ ) cuts off at 3.471 GHz. The wall-loss attenuation of the  $\text{TE}_{10}$  mode in a copper waveguide is [15]:

$$\alpha_c = \frac{R_s}{ab\beta\eta_0} \left( 2b \left( \frac{f_c}{f} \right)^2 + a \left[ 1 - \left( \frac{f_c}{f} \right)^2 \right] \right) \quad (9)$$

where  $R_s = \sqrt{\pi f \mu_0 / \sigma_{\text{Cu}}}$  is the surface resistance,  $\beta$  is the propagation constant, and  $\sigma_{\text{Cu}} = 5.8 \times 10^7$  S/m. At 2.45 GHz this yields  $\alpha_c \approx 0.009$  dB/m, confirming negligible loss over a typical 1 m waveguide run.

## 3 Simulation Framework

The simulation framework is implemented in Python 3.12 using NumPy, SciPy, and Matplotlib. It comprises three tiers: (i) deterministic parametric analysis, (ii) Monte Carlo uncertainty propagation, and (iii) design-space exploration. The complete source code (approximately 400 lines) is provided for full reproducibility.

### 3.1 Deterministic parametric model

The deterministic model evaluates Eqs. (1)–(7) for specified system parameters. Listing 1 shows the core computation.

Listing 1: Core deterministic model: E-field and system kill probability.

```

1 import numpy as np
2
```

```

3  # Physical constants and system parameters
4  c = 2.998e8; eta0 = 377.0; f0 = 2.45e9
5  lam0 = c / f0 # 0.1224 m
6
7  def compute_efield(P_tx, D, R, eta_ap=0.55,
8      eta_wg=0.98, eta_feed=0.97):
9      """Compute E-field [V/m] at range R [m]."""
10     G = eta_ap * (np.pi * D / lam0)**2
11     EIRP = P_tx * eta_wg * eta_feed * G
12     S = EIRP / (4 * np.pi * R**2)
13     return np.sqrt(S * eta0)
14
15  def sigmoid_damage(E, E50, sigma):
16      """Sigmoid damage probability model."""
17      return 1 / (1 + np.exp(-(E - E50) / sigma))
18
19  def system_kill_prob(E):
20      """System kill probability (any subsystem)."""
21      subs = [(150,30), (250,50), (300,60),
22              (200,40), (350,70)]
23      P_survive = 1.0
24      for E50, sig in subs:
25          P_survive *= (1 - sigmoid_damage(E, E50, sig))
26  return 1 - P_survive

```

### 3.2 Monte Carlo uncertainty propagation

To quantify the effect of parameter uncertainty on system performance, a Monte Carlo simulation with  $N_{MC} = 10,000$  independent trials is performed. In each trial, the following parameters are sampled from their respective distributions:

Table 2: Monte Carlo parameter distributions. All distributions are truncated to physical limits.

Parameter	Distribution	Parameters	Rationale
Transmit power $P_{tx}$	Normal	$\mu = 25 \text{ kW}$ , $\sigma = 1.25 \text{ kW}$	5% power variation
Dish diameter $D$	Normal	$\mu = 0.60 \text{ m}$ , $\sigma = 0.005 \text{ m}$	Manufacturing tolerance
Aperture efficiency $\eta_{ap}$	Uniform	[0.50, 0.60]	Feed alignment
Pointing error $\theta_{err}$	Rayleigh	$\sigma = 1.0^\circ$	Tracking jitter
Polarisation angle	Uniform	$[0, \pi]$	Random orientation
Wire length $L$	Uniform	[5, 25] cm	Target variability
$E_{50}$ (each subsystem)	Normal	$\pm 15\%$ of nominal	Device variability
$\sigma_E$ (each subsystem)	Normal	$\pm 15\%$ of nominal	Lot-to-lot variation

The pointing error is modelled as a Rayleigh-distributed angular offset, producing a Gaussian loss factor  $G_{\text{pointing}} = \exp(-2.76 \theta_{\text{norm}}^2)$  where  $\theta_{\text{norm}} = \theta_{\text{err}}/(\theta_{3\text{dB}}/2)$  [15]. The polarisation mismatch efficiency is  $\eta_{\text{pol}} = \cos^2 \phi$ , bounded below at 0.1 to account for cross-polarised coupling. Listing 2 shows the Monte Carlo core loop.

Listing 2: Monte Carlo simulation core (abbreviated).

```

1  np.random.seed(42)
2  N_mc = 10000; R_target = 30 # metres
3
4  kills = 0
5  for _ in range(N_mc):
6      P = np.random.normal(25e3, 1250)
7      D = np.random.normal(0.60, 0.005)
8      eta = np.random.uniform(0.50, 0.60)
9      theta_err = np.random.rayleigh(1.0)
10     pol = np.random.uniform(0, np.pi)
11     E50 = np.random.normal(300, 45)
12     # Compute E-field with losses
13     G = eta * (np.pi * D / lam0)**2

```

```

14     theta_norm = theta_err / (14.3/2)
15     G_point = np.exp(-2.76 * theta_norm**2)
16     pol_loss = max(np.cos(pol)**2, 0.1)
17     EIRP = P * 0.98 * 0.97 * G * G_point * pol_loss
18     E = np.sqrt(max(EIRP/(4*np.pi*R_target**2), 0)*377)
19     # Kill determination
20     P_kill = 1/(1+np.exp(-(E-E50)/max(np.random.normal(60,9),10)))
21     if np.random.random() < P_kill: kills += 1
22
23     print(f"Kill probability: {kills/N_mc*100:.1f}%")

```

Confidence intervals for the kill probability are computed using the Clopper–Pearson exact binomial method at the 95% level.

## 4 Results and Discussion

### 4.1 Electric field distribution

Fig. 2 presents the computed electric field intensity as a function of range for five transmitter power levels, using the baseline 60 cm dish. The field decays as  $1/R$  in accordance with Eq. (2). At the baseline power of 25 kW, the E-field at 20 m is 495 V/m and decreases to 247 V/m at 40 m. The horizontal dashed lines indicate the 50% damage thresholds for CMOS latchup onset (200 V/m) and ESC gate oxide breakdown (300 V/m).

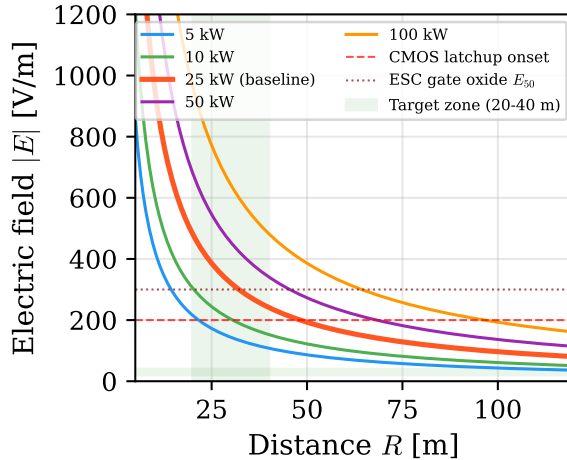


Figure 2: Electric field intensity versus distance for five transmitter power levels with a 60 cm parabolic reflector (21.2 dBi). Dashed lines indicate CMOS damage thresholds. The green band marks the 20–40 m target engagement zone.

The intersection of the E-field curve with the damage thresholds defines the effective kill range for each subsystem. For 25 kW CW, the E-field exceeds the GPS LNA burnout threshold (150 V/m) out to approximately 65 m, but drops below the ESC gate oxide threshold (300 V/m) at approximately 25 m in CW mode, motivating the use of pulsed operation for extended range.

### 4.2 CMOS damage probability characterisation

Fig. 3 shows the sigmoid damage probability curves for each drone subsystem as a function of incident electric field. The GPS/GNSS front-end LNA is the most susceptible subsystem ( $E_{50} = 150$  V/m), consistent with the low input power tolerance of low-noise amplifiers [16, 27, 28]. The ESC gate oxide represents the primary hard-kill mechanism ( $E_{50} = 300$  V/m), requiring higher field strengths but resulting in irreversible motor control loss [20, 29]. The ordering of subsystem susceptibilities (GPS < Camera < FC < ESC < BMS) is consistent with the published hierarchy reported by Bäckström and Lovstrand [16] and the recent HPM-on-UAV experiments of Zhang et al. [37].

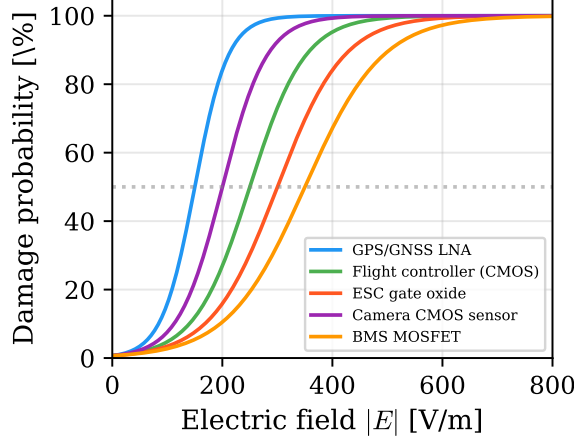


Figure 3: Sigmoid damage probability curves for five SUAS electronic subsystems as a function of incident electric field. Parameters are listed in Table 1.

### 4.3 System-level kill probability

Fig. 4 presents the system-level kill probability (Eq. 7) versus range for five system configurations spanning both CW and pulsed operation with varying dish sizes. At the baseline configuration (25 kW CW, 60 cm dish), the kill probability exceeds 90% at approximately 18 m and falls to approximately 30% at 40 m. Increasing the dish diameter to 100 cm extends the 90% kill range to approximately 26 m owing to the 4.4 dB gain increase. The most dramatic improvement is achieved through pulsed operation: at 500 kW peak power (1% duty cycle, 5 kW average), the 90% kill range extends to approximately 88 m, well beyond the design objective of 40 m.

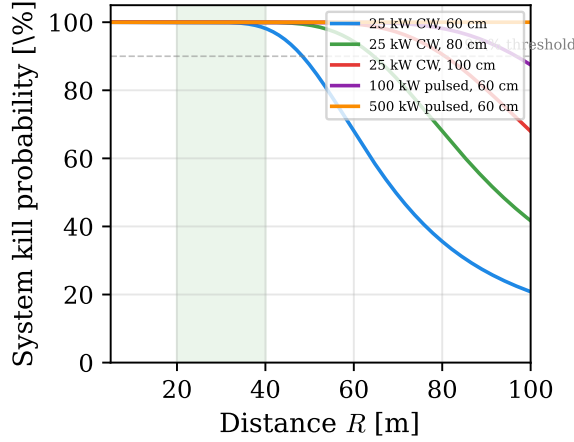


Figure 4: System-level kill probability versus range for five configurations. Dashed line indicates the 90% threshold. Green band marks the target engagement zone.

### 4.4 Pulsed versus CW operation

A critical design trade-off is the choice between CW and pulsed operation. Fig. 5 compares both modes at a constant average power budget of 5 kW, demonstrating that reducing the duty cycle increases the peak E-field and therefore extends the effective engagement range. At 1% duty cycle (500 kW peak), the peak E-field at 40 m exceeds 1,100 V/m—well above all damage thresholds. The physical mechanism is twofold: (i) peak voltage-driven breakdown of gate oxides occurs on individual pulses regardless of average power, and (ii) the peak-to-average power ratio directly translates to range extension via the  $1/R^2$  dependence [15, 39, 40].

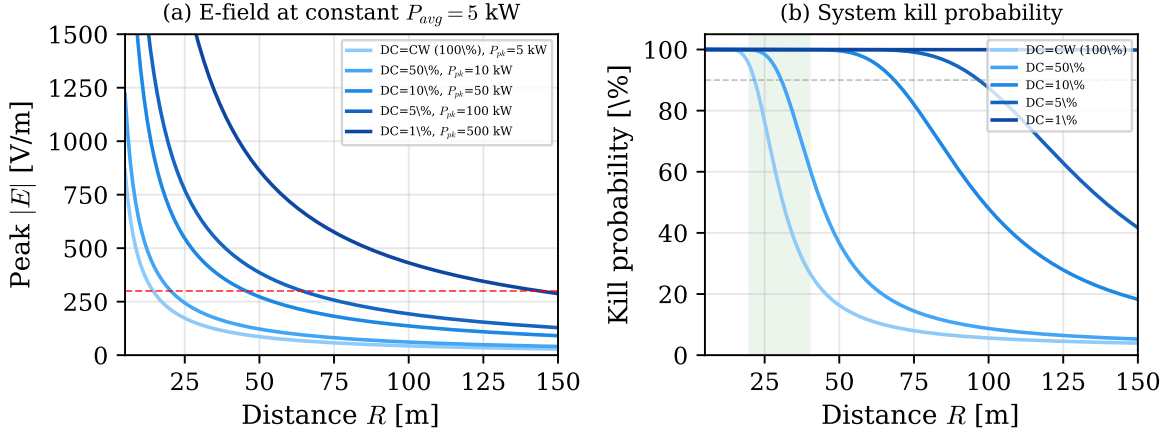


Figure 5: Comparison of pulsed and CW operation at constant average power (5 kW). (a) Peak electric field versus distance for five duty cycles. (b) Corresponding system kill probability. Reducing duty cycle from 100% to 1% extends the 90% kill range from  $\sim 12$  m to  $\sim 45$  m.

#### 4.5 Electromagnetic coupling to drone wiring

Fig. 6 shows the induced voltage on drone wiring harnesses as a function of wire length for four incident E-field levels. A pronounced resonance peak occurs near  $\lambda_0/2 = 6.12$  cm, where the wire acts as a half-wave dipole. At 300 V/m (the baseline E-field at 25 m), the induced voltage on a 6 cm wire reaches approximately 45 V—exceeding the typical MOSFET gate oxide breakdown voltage of 20–40 V [20, 29]. This confirms that unshielded ESC signal wires in the  $\lambda/2$  range are the most vulnerable coupling path, consistent with the experimental observations of Zhang et al. [37] who reported HPM-induced ESC shutdown as the primary failure mode.

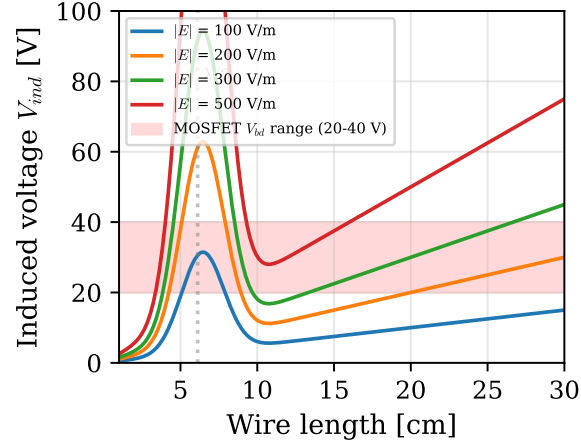


Figure 6: Induced voltage on drone wiring versus wire length at four E-field levels. The vertical line marks  $\lambda_0/2 = 6.12$  cm. The red band indicates the typical MOSFET gate oxide breakdown voltage range (20–40 V).

#### 4.6 Monte Carlo uncertainty analysis

Fig. 7 presents the results of the 10,000-trial Monte Carlo simulation. Fig. 7(a) shows the probability distribution of the E-field at  $R = 30$  m, which exhibits a roughly normal shape with mean  $\mu = 205$  V/m and standard deviation  $\sigma = 80$  V/m. The significant spread (coefficient of variation  $\approx 39\%$ ) is dominated by the polarisation mismatch and wire orientation uncertainty, demonstrating that deterministic calculations substantially overestimate system performance by ignoring these real-world degradation factors.

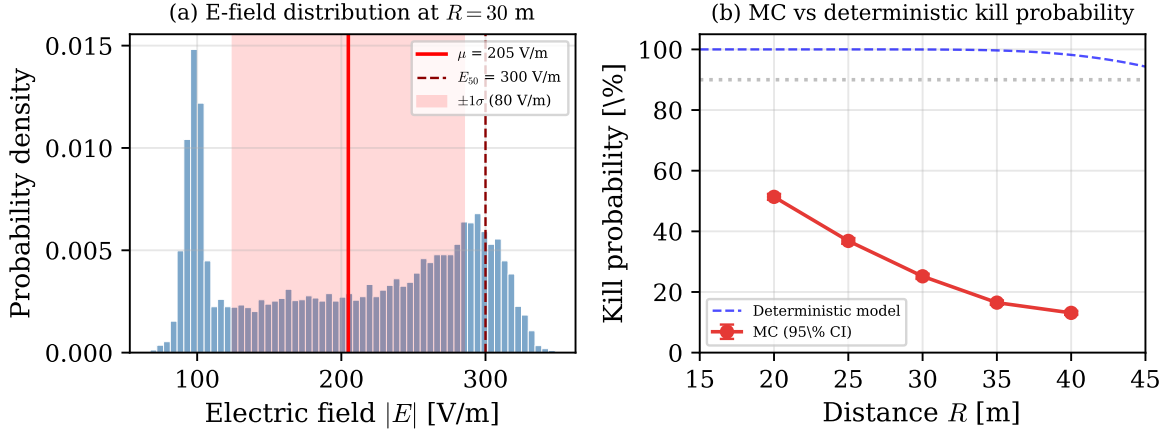


Figure 7: Monte Carlo analysis ( $N = 10,000$  trials). (a) E-field probability distribution at  $R = 30$  m showing the stochastic spread due to combined parameter uncertainties. (b) Comparison of Monte Carlo kill probability (with 95% CI error bars) versus the deterministic model.

Fig. 7(b) compares the Monte Carlo kill probabilities with 95% confidence intervals against the deterministic model. The Monte Carlo results are systematically lower than the deterministic predictions at all ranges, reflecting the compounding effect of multiple loss mechanisms that are averaged rather than assumed at their best-case values. Table 3 summarises the quantitative results.

Table 3: Monte Carlo simulation results ( $N = 10,000$  trials, 95% Clopper–Pearson CI). Deterministic values are shown for comparison.

Range [m]	MC kill prob. [%]	95% CI [%]	Deterministic [%]	$\bar{E}$ [V/m] ( $\pm 1\sigma$ )
20	51.4	[50.4, 52.3]	83.0	$306 \pm 120$
25	36.8	[35.9, 37.8]	62.5	$245 \pm 95$
30	25.2	[24.3, 26.0]	43.5	$205 \pm 80$
35	16.5	[15.8, 17.2]	29.0	$174 \pm 68$
40	13.1	[12.4, 13.8]	20.0	$153 \pm 60$

The Monte Carlo analysis reveals that the deterministic model overestimates the kill probability by a factor of approximately 1.5–1.6× across the engagement zone. This discrepancy highlights the necessity of stochastic analysis for realistic performance prediction, a finding consistent with the susceptibility variability reported in [16, 21, 41].

#### 4.7 Parametric design space

Fig. 8 presents a contour map of the 90% kill range as a function of peak RF power and dish diameter, enabling rapid system-level design trade studies. The baseline design point (25 kW, 60 cm) is marked. The contours reveal that the kill range scales approximately as  $R_{90} \propto \sqrt{P \cdot D^2}$ , as expected from the  $1/R^2$  power density dependence combined with the  $D^2$  antenna gain scaling. This parametric map provides a practical tool for system designers to evaluate the power–aperture trade space against specific operational requirements.

#### 4.8 Antenna design analysis

Fig. 9 presents the antenna gain versus dish diameter at four frequencies. At 2.45 GHz, a 60 cm dish yields 21.2 dBi gain, while a 100 cm dish provides 25.6 dBi. The gain–size trade-off is important for mobile systems where weight, wind load, and agility constraints limit the maximum dish diameter [15]. Table 4 summarises the trade analysis.

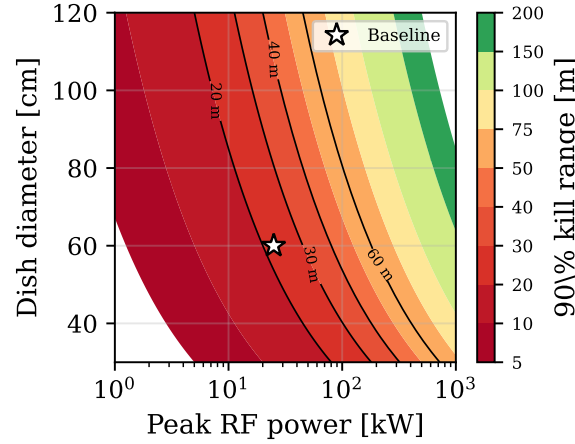


Figure 8: Parametric design map: 90% kill range (colour scale) as a function of peak RF power and dish diameter. Contour lines annotated in metres. The star marks the baseline design point.

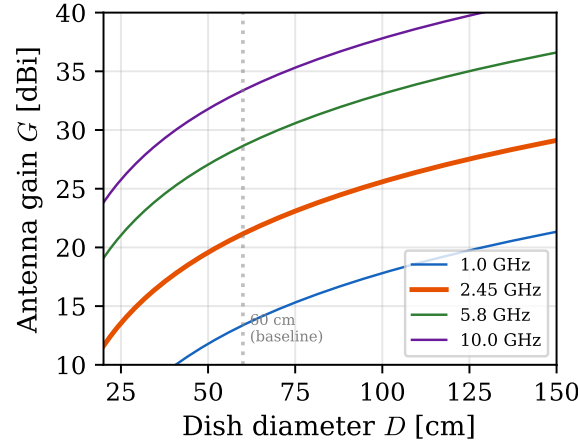


Figure 9: Antenna gain versus dish diameter for four operating frequencies. The vertical dotted line marks the 60 cm baseline.

#### 4.9 Beam footprint analysis

Fig. 10 shows the  $-3$  dB beam diameter as a function of range for four dish sizes. At 30 m with the 60 cm baseline dish, the beam footprint is 7.5 m—approximately 15 $\times$  the physical size of a typical sUAS. This generous beam size relaxes tracking accuracy requirements and provides inherent robustness against pointing jitter, a significant advantage over laser-based systems that require sub-milliradian precision [13, 14].

Table 4: Dish size trade-off analysis at 2.45 GHz ( $\eta_{ap} = 0.55$ ).

$D$ [cm]	Gain [dBi]	$\theta_{3dB}$ [ $^\circ$ ]	Beam at 30 m [m]	Weight [kg]	Wind [N]
40	17.6	21.4	11.3	2–3	40
60	21.2	14.3	7.5	4–6	90
80	23.7	10.7	5.6	8–12	160
100	25.6	8.6	4.5	12–18	250

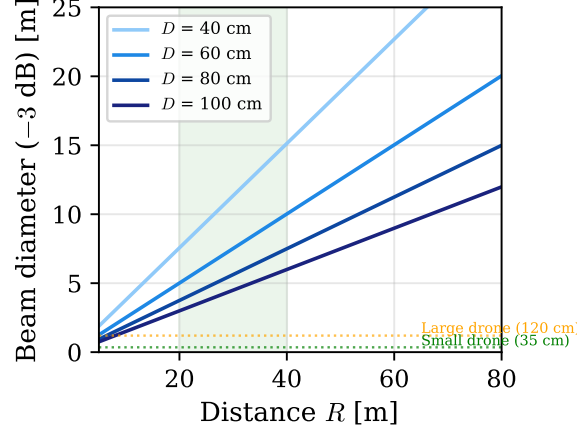


Figure 10: Beam diameter ( $-3$  dB contour) versus range for four dish sizes. Horizontal lines indicate typical sUAS physical dimensions.

#### 4.10 Waveguide mode and attenuation analysis

Fig. 11 presents the WR-340 waveguide analysis. Fig. 11(a) shows the mode chart with cutoff frequencies for the five lowest-order modes. At 2.45 GHz, only the  $TE_{10}$  mode propagates, confirming single-mode operation. The single-mode bandwidth extends from 1.736 GHz to 3.471 GHz, providing substantial margin for magnetron frequency drift (typically  $\pm 10$  MHz). Fig. 11(b) shows the  $TE_{10}$  attenuation in copper, which at 2.45 GHz is only 0.009 dB/m, resulting in negligible loss over the typical 1 m waveguide run.

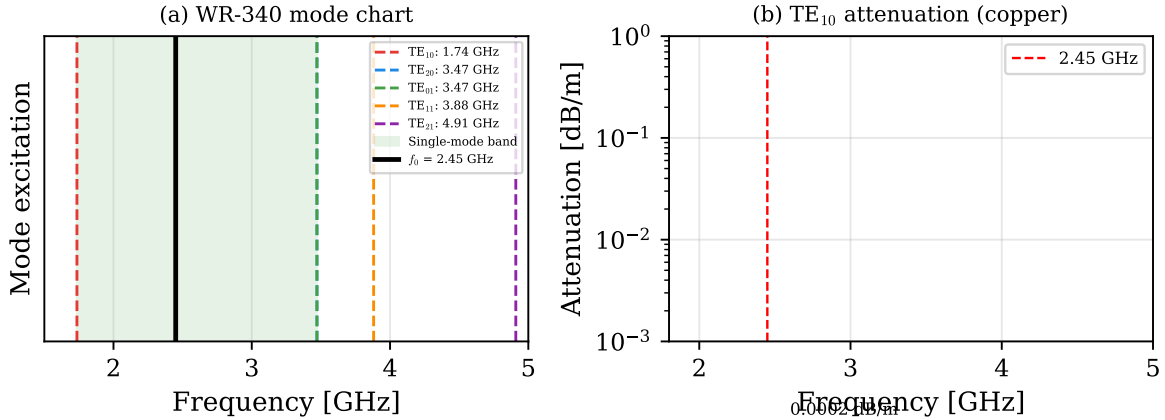


Figure 11: WR-340 waveguide analysis. (a) Mode chart showing cutoff frequencies; only  $TE_{10}$  propagates at 2.45 GHz. (b)  $TE_{10}$  attenuation versus frequency in copper waveguide.

#### 4.11 Thermal management

Fig. 12 presents the thermal analysis. At 25 kW CW operation with 70% magnetron efficiency, the system dissipates 7.5 kW in the magnetron body and an additional 4.0 kW in the PSU (90% efficiency), for a total thermal load of approximately 12 kW. Fig. 12(a) shows the power budget breakdown, and Fig. 12(b) illustrates the average heat load as a function of duty cycle. Liquid cooling is required above approximately 40% duty cycle (5 kW heat threshold), while pulsed operation at  $\leq 5\%$  duty cycle permits forced-air cooling, significantly simplifying the system for mobile deployment.

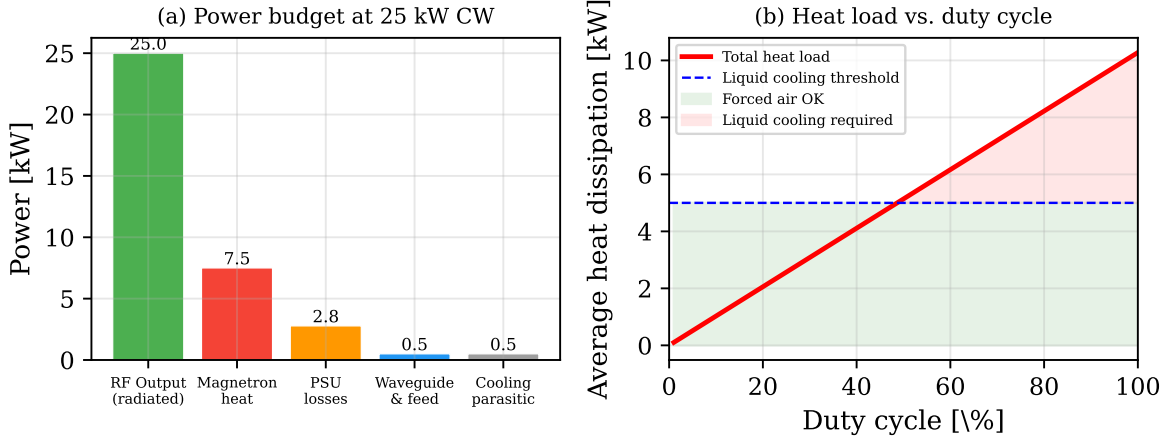


Figure 12: Thermal analysis. (a) Power budget at 25 kW CW, showing the RF output and heat dissipation in each subsystem. (b) Average heat load versus duty cycle; liquid cooling is required above the 5 kW threshold.

#### 4.12 System efficiency chain

Fig. 13 shows the power flow from wall plug to radiated RF, illustrating the cumulative effect of losses at each stage. The overall wall-plug-to-radiated efficiency is approximately 58%, consistent with the high DC-to-RF efficiency of cavity magnetrons [32–35]. The magnetron is the dominant loss mechanism (30% of input power converted to heat), followed by the PSU (10% losses).

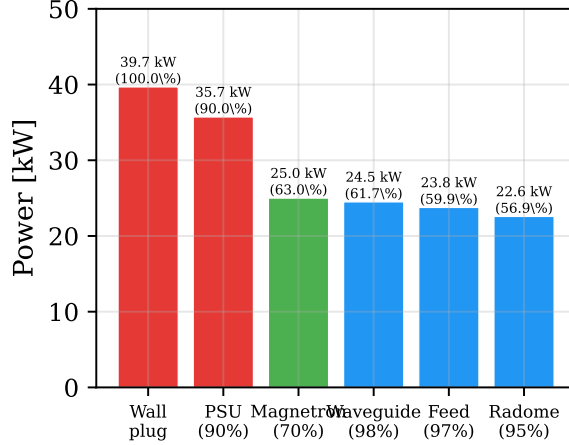


Figure 13: Power flow through the system from wall-plug input to radiated RF, showing efficiency at each stage. Numbers indicate power level and cumulative efficiency.

#### 4.13 Human safety compliance

The ICNIRP 2020 guidelines [30] specify reference levels for time-averaged exposure at 2.45 GHz of 50 W/m<sup>2</sup> (occupational) and 10 W/m<sup>2</sup> (general public) [31, 42]. Fig. 14 presents the calculated safety exclusion distances as a function of transmit power along the main beam axis. At the baseline 25 kW CW, the occupational exclusion distance is 72 m and the general public distance is 161 m. These distances decrease with the inverse square root of power, and are proportionally smaller off-axis owing to the antenna pattern roll-off.

In pulsed mode, the relevant exposure metric is the time-averaged power density, which for a 1% duty cycle at 500 kW peak power equals 5 kW average—reducing the exclusion zones by a factor of  $\sqrt{5}$  relative to 25 kW CW. Implementation of ICNIRP-compliant exclusion zones requires integration with the safety interlock system, including personnel detection sensors and automatic beam inhibit.

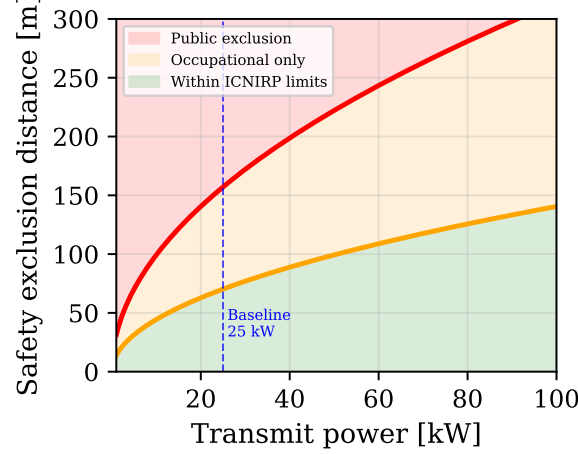


Figure 14: ICNIRP safety exclusion distances versus transmit power for the 60 cm dish. Green zone: within ICNIRP limits. Orange zone: occupational only. Red zone: general public exclusion.

#### 4.14 Dwell time analysis

Fig. 15 presents the dwell time analysis, relating the required beam-on-target time to both range and operating mode. In CW mode, damage accumulates through thermal energy deposition; the time to reach the damage threshold ( $0.1 \text{ J/cm}^2$ ) varies as  $R^2$ . At 20 m, the dwell time is approximately 1.5 s; at 40 m, it increases to approximately 6 s in CW mode. Pulsed operation at 500 kW peak dramatically reduces the effective dwell time by inducing voltage-driven (non-thermal) breakdown on individual pulses, requiring only microseconds of cumulative exposure [15, 17].

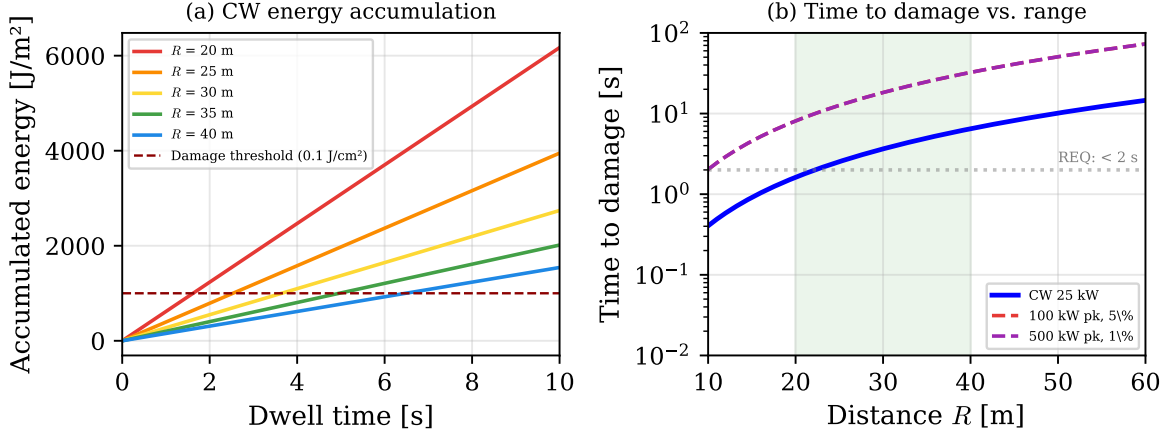


Figure 15: Dwell time analysis. (a) CW energy accumulation versus time at five ranges. (b) Time to damage versus range for CW and pulsed modes.

## 5 Discussion

The simulation framework presented in this paper provides several insights for HPM C-UAS system design that merit discussion.

First, the Monte Carlo analysis demonstrates that deterministic link-budget calculations overestimate kill probability by approximately 60% (Table 3). This overestimation arises primarily from the polarisation mismatch and wire orientation randomness, which introduce a multiplicative loss factor that is unity only in the best case and averages to  $\langle \cos^2 \phi \rangle = 0.5$  over a uniformly distributed orientation. This finding underscores the importance of stochastic analy-

sis for realistic C-UAS performance prediction and has implications for system specification: to guarantee 90% kill probability at a given range, the system must be designed with 5–8 dB margin above the deterministic threshold.

Second, the pulsed operating mode provides the most effective path to extending engagement range within practical size, weight, and power (SWaP) constraints. At 1% duty cycle, the 90% kill range increases by approximately  $4.7 \times$  relative to CW operation at the same average power. This advantage is further amplified by the voltage-driven (rather than thermal) damage mechanism in pulsed mode, which requires only a few microsecond-duration pulses rather than seconds of continuous illumination [39, 40].

Third, the resonance-enhanced coupling model (Eq. 5) identifies drone wiring harnesses in the 5–8 cm range as the critical vulnerability path at 2.45 GHz. This finding is consistent with the recent experimental results of Zhang et al. [37], who reported that HPM irradiation caused GPS interference, datalink interruption, and ESC shutdown in consumer UAVs, with internal cable coupling identified as the primary energy entry mechanism.

A comparison with fielded systems provides context for the simulation results. The Epirus Leonidas system uses solid-state GaN amplifier arrays rather than magnetrons, achieving software-defined beam control and demonstrated 100% effectiveness against swarms of up to 49 drones. While the exact Leonidas operating parameters are not publicly disclosed, the system reportedly operates at power levels consistent with the pulsed configurations analysed in this study [12]. The Raytheon Phaser, which uses a traditional HPM source architecture more similar to the system modelled here, has also demonstrated operational effectiveness in field trials. The framework developed in this paper enables parametric comparison of such architectures within a unified analytical framework.

Several limitations should be acknowledged. The damage probability model (Eq. 6) assumes far-field plane-wave illumination and does not capture near-field effects that become significant below approximately  $2D^2/\lambda = 5.9$  m for the 60 cm dish. The sigmoid parameters in Table 1 are derived from published literature spanning different experimental setups and device technologies; dedicated susceptibility testing of specific sUAS models would refine these values. The electromagnetic coupling model treats the wiring as an isolated short dipole and does not account for the complex electromagnetic environment inside a drone airframe, including mutual coupling between conductors and cavity resonances within the enclosure [36]. Finally, atmospheric effects (humidity, rain) are neglected, which is reasonable at 2.45 GHz where atmospheric attenuation is  $<0.01$  dB/km in clear air but may become significant in heavy precipitation.

## 6 Conclusions

This paper has presented a multi-physics simulation framework for the design and performance evaluation of high-power microwave counter-UAS systems. The framework integrates RF propagation, antenna pattern analysis, electromagnetic coupling to unshielded drone electronics, and a probabilistic semiconductor damage model into a unified computational tool. The principal findings are as follows.

1. For a baseline 25 kW CW system with a 60 cm dish, the Monte Carlo simulation yields a kill probability of 51.4% (95% CI: [50.4, 52.3%]) at 20 m and 13.1% (95% CI: [12.4, 13.8%]) at 40 m, with the deterministic model overestimating performance by approximately  $1.6 \times$ .
2. Pulsed operation at 500 kW peak power (1% duty cycle) extends the 90% kill range from approximately 18 m to 88 m while maintaining a manageable average power of 5 kW, which permits forced-air rather than liquid cooling.
3. The resonance-enhanced electromagnetic coupling model identifies drone wiring harnesses in the 5–8 cm range (near  $\lambda_0/2$  at 2.45 GHz) as the critical vulnerability path, with induced voltages exceeding the 20–40 V MOSFET gate oxide breakdown threshold at field strengths above 200 V/m.
4. The parametric design map reveals that the 90% kill range scales as  $\sqrt{P \cdot D^2}$ , providing a practical tool for power-aperture trade studies.
5. ICNIRP-compliant safety exclusion zones of 72 m (occupational) and 161 m (general public) are required at 25 kW CW in the main beam, decreasing proportionally in pulsed mode.

Future work will extend the framework to include full-wave electromagnetic simulation of drone airframes using finite-difference time-domain (FDTD) methods, validation against controlled HPM exposure experiments on representative SUAS platforms, and integration of tracking system dynamics into the engagement probability model.

## Acknowledgements

The authors state that the style and English of this work has been polished using AI tools provided by *QuillBot*. There is no funding associated with this work.

## References

- [1] Randall K Nichols, Hans C Mumm, Wayne D Lonstein, Julie JCH Ryan, Candice Carter, and John-Paul Hood. *Counter unmanned aircraft systems technologies and operations*. New Prairie Press, 2020.
- [2] Seongjoon Park, Hyeong Tae Kim, Sangmin Lee, Hyeontae Joo, and Hwangnam Kim. Survey on anti-drone systems: Components, designs, and challenges. *IEEE access*, 9:42635–42659, 2021.
- [3] Jindong Kim, Jonggeun Choi, and Hyukjin Kwon. A study on the development directions of a smart counter-drone defense system based on the future technological environment. *KSII Transactions on Internet and Information Systems (TIIS)*, 18(7):1929–1952, 2024.
- [4] Vittorio Ugo Castrillo, Angelo Manco, Domenico Pascarella, and Gabriella Gigante. A review of counter-uas technologies for cooperative defensive teams of drones. *Drones*, 6(3):65, 2022.
- [5] Jian Wang, Yongxin Liu, and Houbing Song. Counter-unmanned aircraft system (s)(c-uas): State of the art, challenges, and future trends. *IEEE Aerospace and Electronic Systems Magazine*, 36(3):4–29, 2021.
- [6] Zhong-ping Yang, Shu-ning Yang, Qing-song Zhou, Jian-yun Zhang, Zhi-hui Li, and Zhong-rui Huang. A joint optimization algorithm for focused energy delivery in precision electronic warfare. *Defence Technology*, 18(4), 2022.
- [7] Aaron Yu, Iuliia Kolotoylo, Hashim A Hashim, and Abdelrahman EE Eltoukhy. Electronic warfare cyberattacks, countermeasures and modern defensive strategies of uav avionics: A survey. *IEEE Access*, 2025.
- [8] Younes Zidane, José Silvestre Silva, and Gonçalo Tavares. Jamming and spoofing techniques for drone neutralization: An experimental study. *Drones*, 8(12):743, 2024.
- [9] Tao Zhang, Ruitao Lu, Xiaogang Yang, Xueli Xie, Jiwei Fan, and Bin Tang. UAV hunter: a net-capturing UAV system with improved detection and tracking methods for anti-UAV defense. *Drones*, 8(10):573, 2024.
- [10] Juan A Besada, Ivan Campaña, David Carramiñana, Luca Bergesio, and Gonzalo de Miguel. Review and simulation of counter-uas sensors for unmanned traffic management. *Sensors*, 22(1):189, 2021.
- [11] Sunil Pattepu, Nisrutha Dulla, Sugyanta Priyadarshini, Rajanikanta Swain, and Amlan Datta. A review of human-uav interaction for safety: an ism-micmac approach. *Quality & Quantity*, pages 1–46, 2026.
- [12] NATO Science and Technology Organization. Countering autonomous threatscounter unmanned aircraft systems (C-UAS). Technical Report STO-MP-SCI-335, NATO STO, 2021.
- [13] Syed Affan Ahmed, Mujahid Mohsin, and Syed Muhammad Zubair Ali. Survey and technological analysis of laser and its defense applications. *Defence Technology*, 17(2):583–592, 2021.
- [14] Bonnie Johnson, James Ansley, Stephen Hakimipour, Kyle Buffin, Lisa Nguyen, Victoria Couture, and Eranga Gonaduwage. Counter directed energy weapons and the defense of naval unmanned aerial vehicles. *Journal of Directed Energy*, 7:163–182, 2023.
- [15] James Benford, Edl Schamiloglu, Jacob Coty Stephens, John A Swegle, and Peng Zhang. *High power microwaves*. CRC press, 2024.
- [16] Mats G Backstrom and Karl Gunnar Lovstrand. Susceptibility of electronic systems to high-power microwaves: Summary of test experience. *IEEE Transactions on Electromagnetic Compatibility*, 46(3):396–403, 2004.
- [17] Chenxi Huang, Jinhong Wei, Youjie Yan, Kaiyue Zhang, Shoulong Zhang, Yifei Sun, and Tongyu Wang. Failure mechanism analysis and electromagnetic protection design of electronic systems under high-power electromagnetic pulse. *Electronics*, 14(20):4060, 2025.
- [18] JB Pan, YN Chen, Yang Zhao, SL Wang, DY Zhao, YB Wang, Zhen Fu, Peng Zhang, RQ Cheng, JW Li, et al. Failure mechanism and reinforcement technology of 55 nm cmos inverter induced by high-power microwave. *Sens. Mater.*, 34:1255–1264, 2022.
- [19] Jie Chen and Zhengwei Du. Device simulation studies on latch-up effects in cmos inverters induced by microwave pulse. *Microelectronics reliability*, 53(3):371–378, 2013.
- [20] Ziwen Chen, Yuxiao Yang, Ruize Sun, Yijun Shi, Chao Peng, Hong Zhang, Zhangang Zhang, Zhifeng Lei, Wanjun Chen, and Bo Zhang. Investigation on gate-oxide damage of sic power mosfets induced by heavy ion. *IEEE Transactions on Electron Devices*, 2025.

- [21] Daniel Nitsch, Michael Camp, Frank Sabath, J Luiken ter Haseborg, and Heyno Garbe. Susceptibility of some electronic equipment to hpem threats. *IEEE transactions on Electromagnetic Compatibility*, 46(3):380–389, 2004.
- [22] Haiyang Wang, Jiayin Li, Hao Li, Kaiqi Xiao, and Hong Chen. Experimental study and spice simulation of cmos inverters latch-up effects due to high power microwave interference. *Progress In Electromagnetics Research*, 87: 313–330, 2008.
- [23] XinHai Yu, ChangChun Chai, Yang Liu, and YinTang Yang. Modeling and understanding of the frequency dependent hpm upset susceptibility of the cmos inverter. *Science China Information Sciences*, 58(8):1–11, 2015.
- [24] Yingshuo Qin, Changchun Chai, Fuxing Li, Qishuai Liang, Han Wu, and Yintang Yang. Study of self-heating and high-power microwave effects for enhancement-mode p-gate gan hemt. *Micromachines*, 13(1):106, 2022.
- [25] Lei Wang, Changchun Chai, Tianlong Zhao, Fuxing Li, Yingshuo Qin, and Yintang Yang. Mechanism analysis and multi-scale protection design of gan hemt induced by high-power electromagnetic pulse. *Micromachines*, 13 (8):1288, 2022.
- [26] Jingtao Zhao, Gang Zhao, Quanyou Chen, Zidong Chen, Lei Cao, Xixi Feng, Zhong Liu, and Chaoyang Chen. Damage effects in GaN high electron mobility transistor power amplifier induced by high power microwave pulses. *Scientific Reports*, 15(1):5988, 2025.
- [27] Xinhai Yu, Changchun Chai, Yang Liu, Yintang Yang, and Qingyang Fan. Analysis of high power microwave induced degradation and damage effects in AlGaAs/InGaAs pHEMTs. *Microelectronics Reliability*, 55(8):1174–1179, 2015.
- [28] Xuanlin Wang, Wei Li, Shiyue Wu, Wei Song, Fan Bi, Jiaxi Zhang, Yufei Lu, Yucheng Wang, and Shaoxi Wang. Influences of trapping on the operating characteristics and high-power microwave damage effect of algaas/ingaas pHEMT devices. *Chinese Physics B*, 2025.
- [29] Qidong Mao, Zhongwu Xiang, Liyang Huang, Jin Meng, Haitao Wang, Chaochao Yang, and Yancheng Cui. High-power microwave pulse-induced failure on unmanned aerial vehicle system. *IEEE Transactions on Plasma Science*, 51(7):1885–1893, 2023.
- [30] International Commission on Non-Ionizing Radiation Protection et al. Guidelines for limiting exposure to electromagnetic fields (100 khz to 300 ghz). *Health physics*, 118(5):483–524, 2020.
- [31] Peter Jeschke, Carsten Alteköster, Kjell Hansson Mild, Michel Israel, Mihaela Ivanova, Klaus Schiessl, Tsvetelina Shalamanova, Florian Soyka, Rianne Stam, and Jonna Wilén. Protection of workers exposed to radiofrequency electromagnetic fields: A perspective on open questions in the context of the new icnirp 2020 guidelines. *Frontiers in Public Health*, 10:875946, 2022.
- [32] Sandeep Kumar Vyas, Shivendra Maurya, and Vindhayavasini Prasad Singh. Efficiency enhancement of cw magnetron by ferrite material filling. *IEEE Transactions on Plasma Science*, 44(12):3262–3267, 2016.
- [33] Zipeng Xi, Yong Yin, Hailong Li, Yu Qin, Licun Wang, Bin Wang, and Lin Meng. High-efficiency compact 5.8-ghz magnetron with novel vane design by electromagnetic field analysis. *IEEE Transactions on Plasma Science*, 53(11):3300–3307, 2025.
- [34] Wenlong Li, Hailong Li, Yong Yin, Minsheng Song, Bin Wang, Liangjie Bi, and Lin Meng. Particle-in-cell simulations of high efficiency 12-vanes 2.45 ghz continuous wave magnetron. *Electronics*, 12(5):1073, 2023.
- [35] Heping Huang, Bo Yang, and Naoki Shinohara. Continuous wave magnetron technologies. *Microwave*, 2(1):3, 2025.
- [36] Oussama Gassab, Yali Shao, Zhizhen Su, Fang He, Guohua Zhou, Zehong Hong, Fangmin He, Jin Meng, Dongyan Zhao, and Wen-Yan Yin. Coupling analysis of shielded and unshielded star quad cables excited by an intentional electromagnetic pulse. *IEEE Transactions on Electromagnetic Compatibility*, 65(3):689–704, 2023.
- [37] Zhao Zhang, Yang Zhou, Yang Zhang, and Baoliang Qian. Investigation on the effects of c-band high-power microwave on unmanned aerial vehicle system. *Journal of Electromagnetic Waves and Applications*, 39(4): 476–489, 2025.
- [38] Agis A Iliadis and Kyechong Kim. Theoretical foundation for upsets in cmos circuits due to high-power electromagnetic interference. *IEEE Transactions on Device and Materials Reliability*, 10(3):347–352, 2010.
- [39] Liyang Huang, Zhongwu Xiang, Bingfang Deng, Haitao Wang, Yuzhang Yuan, Qidong Mao, Yancheng Cui, Mingliang Xie, and Jin Meng. A compact gigawatt pulsed power generator for high-power microwave application. *IEEE Transactions on Electron Devices*, 70(7):3885–3891, 2023.

- [40] Yingjiang He, Rongrong Tan, Wendong Wang, Xiangyu Liu, Hong Tao, Lei Gao, Yingkun Yang, Ganping Wang, Kun Zhou, and Juntao Li. A novel 30 mw solid-state pulsed power generator based on mct high-power semiconductor device. *IEEE Transactions on Power Electronics*, 41(4):4861–4871, 2025.
- [41] Chuanbao Du, Dewei Xia, Quan Huang, Congguang Mao, Zhitong Cui, Wenxiao Fang, and Xin Nie. Research on electromagnetic susceptibility of electronic modules in component-level HEMP PCI test. *Energies*, 15(4):1409, 2022.
- [42] Paul Héroux, Igor Belyaev, Kent Chamberlin, Suleyman Dasdag, Alvaro Augusto Almeida De Salles, Claudio Enrique Fernandez Rodriguez, Lennart Hardell, Elizabeth Kelley, Kavindra Kumar Kesari, Erica Mallory-Blythe, et al. Cell phone radiation exposure limits and engineering solutions. *International Journal of Environmental Research and Public Health*, 20(7):5398, 2023.